DARDAR-CLOUD

DOCUMENT PREPARED BY JULIEN DELANOË

julien.delanoe@latmos.ipsl.fr

AND ROBIN HOGAN

Table of Contents

1. PURPOSE AND SCOPE

This document describes the theoretical basis of the synergetic ice cloud retrieval algorithm that combines the CloudSat radar, the CALIPSO lidar and MODIS measurements: “DARDAR-cloud” and “DARDAR-rad-cloud”, more details can be found in Delanoë and Hogan 2008 and 2010.

The DARDAR-cloud products are routinely processed by the ICARE Data Center (http://www.icare.univ-lille1.fr). A website where is described the product format and content, the version changes and more is maintained at http://www.icare.univ-lille1.fr/projects/dardar/dardar_cloud .

2. OVERVIEW

2.1 Algorithm Name

This algorithm is referred to as **Varcloud**: it uses CloudSat, CALIPSO and MODIS measurements to retrieve the properties of ice clouds within a variational framework. It was developed at the University of Reading by Julien Delanoë and Robin Hogan.

2.2 Name of L2 data Product(s) Generated

The algorithm can generate two products:

- DARDAR-cloud : Ice cloud properties derived from CloudSat and CALIPSO (CALIOP) only.
- DARDAR-rad-cloud: Ice cloud properties derived from CloudSat and CALIPSO (CALIOP) and IR radiances from IIR or MODIS. This product is not routinely available yet.

The variables contained in these products are listed in Table 1 and Table 2 ; note that the format of the two products is the same.

2.3 Description of the L2 data product(s)

The variables contained in the two products are described in detail in Table 1 and Table 2.

Table 1: Description of the L2 data product(s): Attributes

Attributes		
Name	Type	Value
title	8-bit signed char	Optimal estimation ice cloud retrieval method
institution	8-bit signed char	University of Reading, UK: http://www.met.reading.ac.uk
Data Production	8-bit signed	University of Reading, UK: http://www.met.reading.ac.uk

Centre	char	
history	8-bit signed char	Mon Apr 26 12:10:22 2010 - Generated by variational algorithm by sws05jmd on pilvista This Retrieval has been derived from : [Radar reflectivity] [Lidar] Formalism: N0* and N0prime=N0/alpha^coeff Lookup table: /home/sws05jmd/Work/OE/dardar_cloud/LUT/ice_properties_TMatrix_axial_ratio_0_6_BF95_modified_-1_3_cloudsat.cfg Input file: /export/pilvista/raid1/sws05jmd/DARDAR/2006/2006_07_14/DARDAR-MASK_v1.1.2_2006195074445_01121.hdf Check configuration parameters : Configuration for Extinction to backscatter ratio: constant (0), linear vert (1), basis functions (2) :6 N spacing factor :4 Extinction to backscatter ratio spacing factor :4 ln(Extinction to b ackscatter ratio), first guess :3.50 Radius A, first guess :1e-05 ln(Extinction), first guess :-9.00 ln(Extinction to backscatter ratio), apriori :3.50 Smoothscale :1.00 Use molecular signal beyond the cloud (1) otherwise (0) :1 No lidar exploited beyond liquid ...(1) otherwise (0) :1 Diagonal value in a priori errcov :1.00 Ext_bscat_ratio_ice_apriori error 1 :0.10 Ext_bscat_ratio_ice_apriori error 2 :0.00 A priori decorrelation distance :10.00 Z error value in dBZ (forward model):1.00 Beta error value in ln (forward model):0. 30 IR MODIS AQUA(1),IIR(2),SEVERI MSG(3),EARTHCARE MSI(4) :1 Error covariance used, yes (1) no (0) :1 Number of molecular gates used beyond the cloud:5 Nprime a priori as function of Temperature [deg C] (default_logNprime =

		ln(N0*/extinction^coeff) = A +B*T A for Nprime:22.234435 B for Nprime:-0.0907 Nprime coefficient:0.610000 HSRL used ...(1) otherwise (0) :0 IR Wavelength assimilated (micron):11.03 dI=I1-I2 IR (1) Wavelength assimilated for radiance difference (micron):11.03 IR (2) Wavelength assimilated for radiance difference (micron):12.02
Input Files	8-bit signed char	/export/pilvista/raid1/sws05jmd/DARDAR/20 06/2006_07_14/DARDAR-MASK_v1.1.2_2006195074445_01121.hdf
Version	8-bit signed char	1.2.1
Product Name	8-bit signed char	DARDAR_CLOUD
Product Description	8-bit signed char	Varcloud - Optimal estimation ice cloud retrieval method
Institution	8-bit signed char	University of Reading, UK: http://www.met.reading.ac.uk
Data Processing Centre	8-bit signed char	ICARE-CGTD, University of Lille, FR : http://www.icare.univ-lille1.fr
Geographic Projection	8-bit signed char	LIDAR Subtrack
Pixel Size	8-bit signed char	1km
Vertical Bin Size	8-bit signed	60m

	char	
Production Time	8-bit signed char	2010-04-26T12:10:22
Date	8-bit signed char	2006195074445_01121

Table 2: Description of the L2 data product(s): variables

Variables							
Name	type	description	Dimension	Range	Missing value	Fill value	Units
time	Float 32	Time UTC	time (number of profiles)		-999.	-999.	s
latitude	Float 32	Latitude of co-located CloudSat-CALIPSO footprints at the ground	time	[-90 90]	-999.	-999.	degree
longitude	Float 32	Longitude of co-located CloudSat-CALIPSO footprints at the ground	time	[-180 180]	-999.	-999.	degree
vis_optical_depth	Float 32	Visible optical depth, defined as the (dimensionless) line integral of the ice cloud visible extinction along a vertical path through the entire atmosphere.	time	[0 500]	-999.	-999.	none
vis_optical_depth_error	Float 32	Visible optical depth error	time	[0 500]	-999.	-999.	none
height	Float 32	Height above mean sea level, describes the altitude of each radar and lidar (CloudSat-CALIPSO) common range gates	height (436)		-999.	-999.	m

n_iterations	Int 16	Number of iterations before convergence	time x20	[1 20]	-999.	-999.	none
wavelength	Float 32	Wavelength of the centre of radiance channel (infrared)	time x3	[8e-6 14e-6]	-999.	-999.	m
chi2	Float 32	Value of chi squared for each iteration; to determine if the algorithm as converged we use a chi squared convergence test.	time x20	[0 1e6]	1e6	1e6	none
chi2_split	Float 32	Value of chi squared at the final iteration for each measurement type, normalized by the number of gates; the chi2_split dimension indicates the instrument (lidar , Z, radiance, dradiance)	time x6	[0 1e6]	1e6	1e6	none
radiance	Float 32	Forward-modelled radiance. For each infrared radiometer channel, the radiance forward model takes as input the relevant cloud variables from the state vector (profiles of visible extinction coefficient α_v and N_0*) and estimates of other variables (profiles of temperature, pressure, humidity, O_3 and CO_2 concentrations, as well as skin temperature and emissivity). In the case of the DARDAR-cloud product, this calculation is performed on the radar-lidar retrieved profile, while for the DARDAR-rad-cloud product, it is used as part of the retrieval and is calculated at every iteration of the algorithm (although only the value at the final iteration is reported).	time x3	[0 15]	-999.	-999.	W m-2 um-1 sr-1
radiance_sat	Float 32	Radiance from the satellite (channels in wavelength variable)	time x3	[0 15]	-999.	-999.	W m-2 um-1 sr-1
radiance_flag	Int 16	Radiance flag (0 =radiance not used, 1 = radiance used)	time x3	[0 1]	-999	-999	none

radiance_difference_flag	Int 16	Radiance difference flag (0 = radiance not used, 1 = radiance used (first radiance), 2 = radiance used (second radiance), 3 = radiance and radiance difference used)	time x3	[0 3]	-999	-999	none
Z	Float 32	Radar reflectivity	time x height	[1e-4 1e3]	-999.	-999.	mm6 m-3
bscat	Float 32	Lidar attenuated backscatter	time x height	[1e-7 1e-4]	-999.	-999.	m-1 sr-1
DARMASK_Simplified_Categorization	Int 16	DARDAR-categorisation: -9 -> ground -1 -> don't know 0 -> Clear 1 -> ice 2 -> ice + supercooled 3 -> liquid warm 4 -> supercooled 5 -> rain 6 -> aerosol 7 -> maybe insects 8 -> stratospheric feature	time x height	[-9 8]	-9	-9	none
instrument_flag	Int 16	Instrument flag (0==nothing/1==lidar/2==radar/3==radar+lidar)	time x height	[0 3]	-9	-9	none
Z_fwd	Float 32	Forward-modelled 94-GHz radar reflectivity factor	time x height	[1e-4 1e3]	-999.	-999.	mm6 m-3
bscat_fwd	Float 32	Forward-modelled Lidar attenuated backscatter	time x height	[1e-7 1e-4]	-999.	-999.	m-1 sr-1
extinction	Float 32	Retrieved visible extinction coefficient	time x height	[1e-7 1e-1]	-999.	-999.	m-1
lidar_ratio	Float 32	Retrieved extinction-to-backscatter ratio	time x height	[0 100]	-999.	-999.	sr
iwc	Float	Retrieved Ice Water Content, the mass of ice per unit	time x	[1e-9 1e-	-999.	-999.	kg m-3

	32	volume of air	height	2]			
effective_radius	Float 32	Retrieved effective radius, proportional to the ratio of ice water content to visible extinction coefficient	time x height	[0 1e-4]	-999.	-999.	m
N0star	Float 32	Retrieved intercept parameter N0* of the normalized size distribution of ice particles as describe in Delanoë et al. (2005)	time x height	[0 1e14]	-999.	-999.	m-4
ln_extinction_error	Float 32	1-sigma random error in natural logarithm of visible extinction coefficient	time x height	[0 1]	-999.	-999.	ln(m-1)
ln_lidar_ratio_error	Float 32	1-sigma random error in natural logarithm of extinction-to backscatter ratio	time x height	[0 1]	-999.	-999.	ln(sr1)
ln_iwc_error	Float 32	1-sigma random error in natural logarithm of IWC	time x height	[0 1]	-999.	-999.	ln(kg m-3)
ln_effective_radius_error	Float 32	1-sigma random error in natural logarithm of effective radius	time x height	[0 1]	-999.	-999.	ln(m-1)
ln_N0_error	Float 32	1-sigma random error in natural logarithm of normalized number concentration parameter	time x height	[0 1]	-999.	-999.	ln(m-4)
temperature	Float 32	Temperature from ECMWF	time x height	[180 320]	-999.	-999.	K
day_night_flag	Int 16	Day Night Flag for lidar Night (1) Day (0)	time	[0 1]	-9	-9	none
land_water_mask	Int 16	Land Water Mask from Calipso files, indicating the surface type at the laser footprint 0=shallow ocean 1=land 2=coastlines 3=shallow inland water 4=intermittent water 5=deep inland water	time	[0 7]	-9	-9	none

		6=continental ocean 7=deep ocean					

2.4 REQUIRED INPUT DATA

The algorithm currently uses "DARDAR categorisation files" produced at ICARE, which contain all the required observations and thermodynamic variables, interpolated or averaged on to the same grid. Although contained within the same file, here we group the required data into instrument, platform, orbit parameters and meteorological data.

3. ALGORITHM DESCRIPTION

3.1 Introduction

This algorithm uses a variational method for retrieving profiles of visible extinction coefficient, ice water content and effective radius in ice clouds using the combination of radar reflectivity, lidar attenuated backscatter and infrared radiances in the atmospheric water-vapour window. The forward model includes effects such as non-Rayleigh scattering by the radar and molecular and multiple scattering by the lidar.

By rigorous treatment of errors, and a careful choice of state variables and associated *a priori* estimates, a seamless retrieval is possible between regions of the cloud detected by both radar and lidar, and regions detected by just one of these two instruments. Thus, when the lidar signal is unavailable (such as due to strong attenuation), the retrieval tends towards an empirical relationship using radar reflectivity factor and temperature, and when the radar signal is unavailable (such as in optically thin cirrus), accurate retrievals are still possible from the combination of lidar and radiometer.

The algorithm can be used to create two products- "DARDAR-rad-cloud" (using all instruments available), and "DARDAR -cloud" (using only the radar and lidar). It draws heavily from the algorithm developed by Delanoë and Hogan (2008, 2010).

3.2 Physics Background

As explained in detail by Rodgers (2000), variational algorithms (or equivalently those based on "optimal estimation theory"), when properly formulated, have the advantage of being capable of finding the best solution in a least squares sense given all the information available. In the case of the varcloud algorithm, we encapsulate as much physical realism as possible (while still retaining computational efficiency) within the forward models for the various instruments. Thus the microphysical assumptions make use of the most up-to-date information on ice particle size distributions and habits available from aircraft campaigns. This information is stored in the look-up tables described in Table 5. When better aircraft data become available, it can be incorporated by recalculating the elements of the look-up table. The algorithm may then be run on the new tables without the need to be recompiled. The instrument simulators all use physical models of the way radiation interacts with the atmosphere, and in the case of the lidar and infrared radiometer forward models, take full account of attenuation and multiple scattering.

3.3 Algorithm Flow Chart

The description of the algorithm in the subsequent sections is facilitated by the flow chart shown in Figure 1, which outlines the key parts in the way the algorithm works.

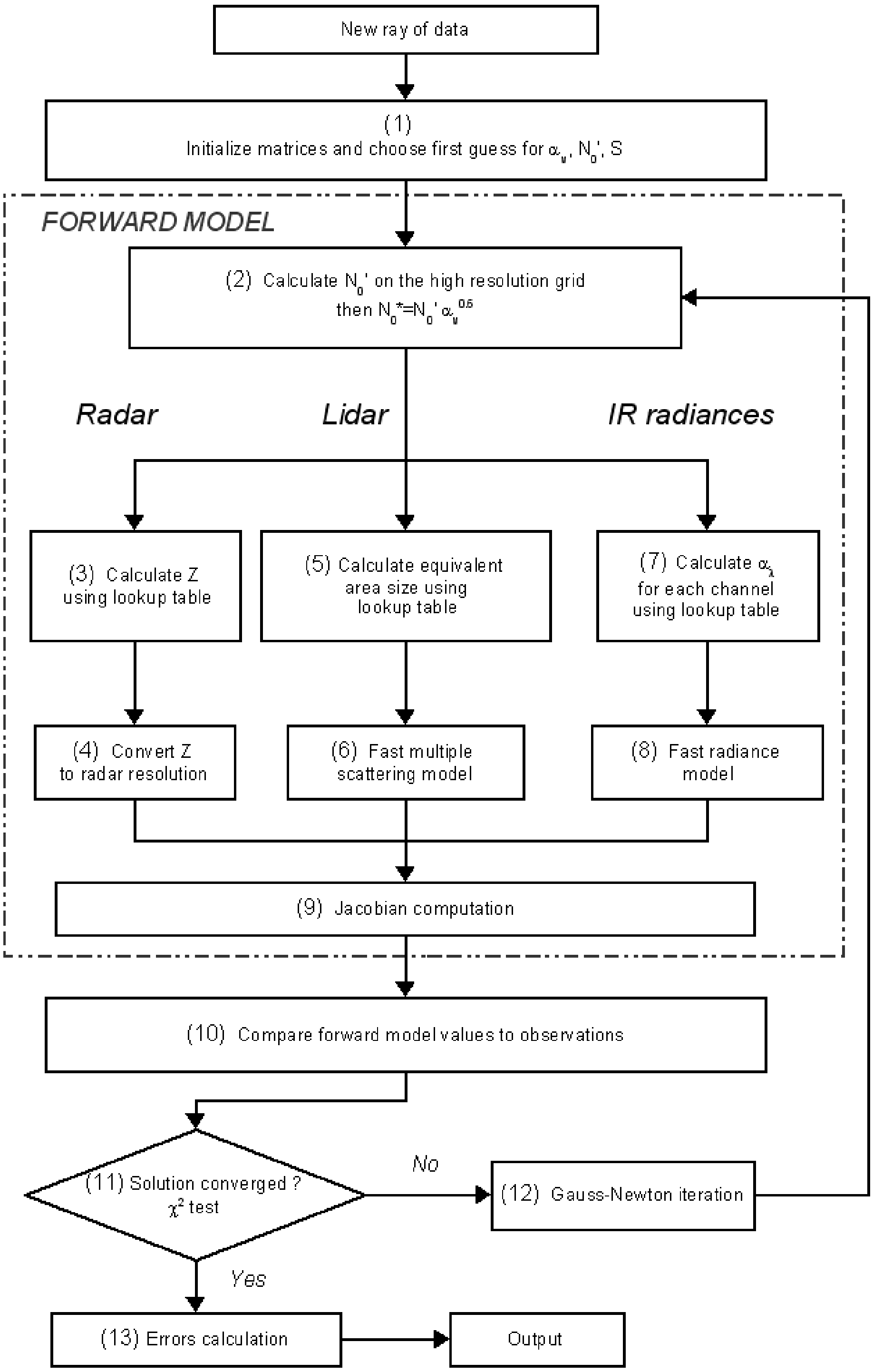

Figure 1: Flowchart showing the sequence of operations performed by the retrieval scheme

3.4 Algorithm Definition

3.4.1 Overview of the variational scheme

We assume that all instruments have been calibrated, that the nature of the random errors in the measurements is known. Profiles are analyzed in turn, and the procedures undertaken for each are summarized in Figure 1. The retrieval is then applied to the parts of the profile containing ice cloud. This is achieved using the target classification (from DARDAR-MASK file), which identifies pixels containing ice and/or liquid. There are two cases when ice clouds are present but the measurements from a particular instrument are unreliable:

- Mixed-phase clouds, typically consist of a layer of liquid water cloud beneath which ice particles are falling. In this situation, the lidar has a large return from the liquid droplets, but is then rapidly extinguished. Since liquid clouds are not currently represented in the state vector or the lidar forward model, in this situation we don't use the lidar pixels within and below the first pixel containing liquid water. Therefore, the ice information within and below the first liquid water layer will originate entirely from the radar. It should be noted that we are neglecting the attenuation of the radar signal by the liquid water cloud, but for supercooled clouds this is generally small. A further possible error to document is that there is some evidence (Hogan et al. 2006a) that when supercooled liquid is present, the ice particles tend to grow more by vapour deposition and riming than by aggregation, leading to them having a higher density for a given size. This could have an impact on the ice water content retrievals, as yet not fully characterized. However, it should be noted that in these situations the liquid water is believed to dominate the radiative properties of the cloud (Hogan et al. 2003) and so the resulting radiative error may not be too significant. Certainly further work is required in this area.

- When liquid clouds are present at any height in the profile (either warm or supercooled), the infrared radiometer observations will contain a contribution from the liquid water that is not represented in the forward model, so cannot be used. Therefore in this situation the radar-lidar-radiometer varcloud algorithm will revert to the behaviour of the radar-lidar varcloud algorithm.

In a variational scheme, one must decide what variables to use to describe the system being observed. These variables will be retrieved and are represented as the *state vector,* $\boldsymbol{x}$. In the case of ice clouds, the visible extinction coefficient, α_v, has the advantage that, in the geometric optics limit, it is directly linked to the both the lidar measurements and to the optical depth of the cloud. For example, in the single-scattering limit and in the absence of molecular scattering, the apparent lidar backscatter at range r from the instrument can be expressed as

$$\beta(r) = \hat{\beta}(r)\exp\left[-2\int_0^r \alpha_v(r')dr'\right], \tag{1}$$

where $\hat{\beta}$ is "true" lidar backscatter coefficient, assumed proportional to α_v via the extinction-to-backscatter ratio, S:

$$\hat{\beta} = \alpha_v / S. \quad (2)$$

Hence the second variable to be added to the state vector is S. In practice, (1) is replaced by a formulation including molecular and multiple scattering, as described in a next section. S is usually assumed constant in radar-lidar algorithms (e.g. [Donovan et al. (2005), Tinel et al. (2005)]). However this strong constraint can be relaxed when the number of independent measurements allows it, for instance the infrared radiances (Delanoë and Hogan 2010).

In order to relate α_v to other moments of the size distribution such as radar reflectivity factor (Z) or ice water content (IWC), it needs to be supplemented in the state vector by another intensive or extensive variable, such as a measure of particle size or number concentration. This additional variable should ideally have two key properties. Firstly, a good *a priori* estimate of it should be available as a function of temperature. This ensures that in regions where only the radar or the lidar is available, the scheme will tend towards existing empirical relationships involving temperature, such as the formulae for IWC as a function of Z and temperature (e.g. Liu and Illingworth 2000, Hogan et al. 2006a, Protat et al. 2007).

It was demonstrated by Hogan et al. (2006a) that the temperature dependence in these relationships must arise via the temperature dependence of the number concentration parameter of a size distribution, commonly referred to as N_0. Secondly, it should be easy to combine this additional variable with α_v to estimate any other property of the size distribution. A good candidate is the ice "*normalized* number concentration parameter", N_0^*. For a full description of the properties of this variable (including to what it is normalized), the reader is referred to Delanoë et al. (2005), but for our purposes, the key property that we exploit is that for any intensive variable y and extensive variable Y there is a near-unique relationship between the ratio α_v / N_0^* and both y and the ratio Y / N_0^*.

Given these requirements, the last variable we add to the state vector is N_0', defined as

$$N_0' = N_0^* / \alpha_v^{0.61}. \quad (3)$$

In Figure 3, it is shown that this mathematical combination of variables has the useful property of being independent of ice water content; unfortunately we do not currently have a good physical reason why this is the case. As shown in section 3.4.7.2, this variable is found to have a strong temperature dependence. Furthermore, N_0^* can easily be derived from the combination of α_v and N_0', which then enables any intensive or extensive variable to be estimated (see section 3.4.7.2).

To improve the computational efficiency, we seek to reduce the number of elements in $\boldsymbol{x}$. Naturally, α_v is only retrieved at the n ranges where ice cloud is detected by either the radar or the lidar. This is achieved using the "DARMASK_Simplified_Categorization", "Target_Radar_Mask" and "Target_Lidar_Mask" variables (greater or equal to 1) from DARDAR-MASK file. An additional efficiency is obtained by not retrieving N_0' directly at each gate, but rather representing it by reduced set of m basis functions, N_b, such that smooth variation in range is guaranteed. The same approach was used by Hogan (2007) to retrieve an analogous variable for polarization radar measurements in rain. Consequently, the state vector for a single profile is

$$\boldsymbol{x} = \begin{pmatrix} \ln \alpha_{v,1} \\ \vdots \\ \ln \alpha_{v,n} \\ \ln S_1 \\ \vdots \\ \ln S_g \\ \ln N_{b,1} \\ \vdots \\ \ln N_{b,m} \end{pmatrix}. \qquad (4)$$

Note that we use the logarithm of the entities α_v, N_b and S, not the entities themselves, to avoid the unphysical possibility of retrieving negative values. In section 3.4.4, we describe the S retrieval assumptions, however for the sake of convenience we express the state vector with ln$S$ with an index varying between 1 and g.

With the state vector now defined, we turn to the *observation vector,* ***y***. This contains the measurements Z (the radar reflectivity factor), β (the apparent lidar backscatter), I_λ (the infrared radiance at wavelength λ) and ΔI (the difference between two infrared radiances). Currently the default is to use the combination 11 and 12 microns. Radiances measured in the infrared atmospheric window provide information on the extinction of the cloud within the nearest one or two optical depths, provided that the temperature profile is well known. The difference between two infrared radiances provides information on ice particle size [Chiriaco et al. (2004), Cooper et al. (2003)].

Hence, the observation vector can be written as

$$\boldsymbol{y} = \begin{pmatrix} \ln \beta_1 \\ \vdots \\ \ln \beta_p \\ \ln Z_1 \\ \vdots \\ \ln Z_q \\ I_\lambda \\ \Delta I \end{pmatrix}. \qquad (5)$$

Note that β and Z have different indices p, and q, since the radar and lidar usually do not sample exactly the same part of the cloud. The lidar signal is more sensitive to the concentration of the particles but can be extinguished when the cloud becomes too thick (typically when optical depth is greater than 3). The radar is more sensitive to the size of the particles and therefore does not always detect very optically thin clouds. It is advantageous to include in ***y*** any gates beyond the far end of the cloud, this enables any molecular return measured here to be used automatically as a constraint on optical depth [Cadet et al.(2005)].

When liquid is detected within the profile, the lidar signal is not used in the retrieval below this liquid pixel even if there is ice, because in this ice-cloud algorithm liquid is not represented in the state vector or the forward model, and so it is not possible to correctly interpret the lidar measurements in such a situation.

Therefore in this situation, the radar alone is used to retrieved ice cloud properties. If measurements are missing they are simply excluded from ***y***. As in the state vector, the logarithms of the entities β and Z are used because of the large dynamic range that they can span in a single profile. It is also found that the use of logarithms in ***x*** and ***y*** results in much faster convergence to the correct solution.

The slowest part of the radar-lidar-radiometer retrieval is currently in the forward model for the radiometer. Therefore, in practice, the retrieval is performed in two parts: the first in which the I_λ and ΔI elements are omitted from ***y***, and a radar-lidar retrieval is iterated until convergence. The retrieved ice cloud properties are then used as the first guess for a second part in which the I_λ and ΔI elements are reintroduced into ***y***, and the iterations are continued but including forward modelling of the radiance quantities. In practice it is found that only a few further iterations are necessary at this point, since the radar-lidar combination usually derives a profile very close to the final profile from all three instruments. In producing the "DARDAR cloud properties" product, we simply stop the retrieval after the first part and report the ice cloud properties retrieved only by the radar-lidar combination. By default, we use the 11 micron channel for I_λ and the 11 and 12 combination for ΔI, although it is straightforward to change this. The reason for using ΔI rather than two radiances I_{11} and I_{12} independently is that the forward modelling of the radiances is subject to errors in the temperature profile, and both radiances will be affected in the same way. This has the effect of introducing an observational error correlation between these two measurements, but unfortunately that is very difficult to characterise and indeed no observational error correlations are included in the formulation of the retrieval (i.e. the observational error covariance matrix **R** is diagonal). This problem can be overcome to some extent by taking the difference between two radiances ΔI.

3.4.2 Optimal estimation formulation

The essence of the technique is to start with a first guess of the state vector and use a *forward model* (represented by the dot-dashed box in Figure 1) to predict each element of the observation vector. This prediction is compared to the actual observations (box 10 of Figure 1) and the difference is used to calculate a refined state vector that is fed back into the forward model. This process is repeated until convergence. The aim is to find the state vector that minimizes the difference between the observations and the forward model in a least-squares sense. This is achieved by minimizing a cost function J :

$$2J = \sum_{i=1}^{q} \frac{\left(\ln Z_i - \ln Z_i'\right)^2}{\sigma^2_{\ln Z_i}} + \sum_{i=1}^{p} \frac{(\ln \beta_i - \ln \beta_i')^2}{\sigma^2_{\ln \beta_i}}$$

$$+ \frac{\left(I_\lambda - I_\lambda'\right)^2}{\sigma^2_{I_\lambda}} + \frac{\left(\Delta I - \Delta I'\right)^2}{\sigma^2_{\Delta I}}$$

$$+ \sum_{i=1}^{n+m+g} \frac{\left(x_i - x_i^a\right)^2}{\sigma^2_{a,i}}. \tag{6}$$

The first five elements on the right hand side of (6) represent the deviation of the observations ln Z, ln β, I_λ and ΔI, from the values predicted by the forward model ln Z', ln β', I_λ' and $\Delta I'$, with the root-mean-squared (RMS) observational errors represented by $\sigma_{\ln Z}$, $\sigma_{\ln\beta}$, $\sigma_{I\lambda}$ and $\sigma_{\Delta I}$. In practice these include forward-model errors as discussed in sections 3.4.6 and 3.4.7.4.

The last summation in (6) represents the deviation of the elements of the state vector from some *a priori* estimate, x^a (referred to as the "background" in data assimilation). This term assists in the stability of the algorithm and ensures that if radar or lidar observations are missing then the retrieval will tend towards the behavior of existing empirical algorithms in the literature. In most cases, an *a priori* is only required for N_0' (see section 3.4.7.2) and *S*, not for α_v since this variable is well constrained by both radar and lidar. Note that although the natural logarithm of several quantities is taken in (6), this should not lead to small deviations being weighted incorrectly with respect to large deviations, because each deviation is normalized by its error variance, which is rigorously calculated in each case.

However, it is found to be useful to use for α_v but with a large error, as this ensures the stability of the retrieval in a very small fraction of cases where this is necessary, but without significantly affecting the results in the vast majority of cases. A wide range of values of *S* have been reported in the literature; following the evidence of Platt et al. (1987) and Chen et al. (2002) of S typically varying between 20 sr and 60 sr, Platt et al. [2002] show that for very cold ice clouds, S can go up to 100 sr.

Table 3: First guess and a-priori for the state vector

Variable	Description	First guess and a-priori	A-priori error	Unit
ln S	Extinction-to-backscatter ratio	As a function of temperature	0.5	ln(sr)
ln α_v	Extinction coefficient; an a priori is usually not required but is used to stabilize the retrieval in a very small fraction of cases, so we set a large error to the a priori.	$\ln(10^{-6})$	5.0	$\ln(m^{-1})$
ln N0'	The a-priori for this variable is defined as ln(N0') = $\ln(N0^*/\text{extinction}^{0.6})$ =A +B*T, where temperature T is in degree Celsius.	A =22.234435 B=-0.0907	1	$\ln(m^{-3.4})$

In order to incorporate error correlations and smoothness constraints, it is convenient to rewrite (6) in matrix notation:

$$2J = \delta y^T R^{-1} \delta y + \delta x_a^T B^{-1} \delta x_a + x^T T x \qquad (7)$$

where $\boldsymbol{\delta y}=\boldsymbol{y}-H(\boldsymbol{x})$, $\delta \mathbf{x_a}=\mathbf{x}-\mathbf{x^a}$, $H(\boldsymbol{x})$ is the forward model operator, and $\boldsymbol{R}$ and $\boldsymbol{B}$ are the error covariance matrices of the observations and the *a priori,* respectively. In this application we assume that $\boldsymbol{R}$ is diagonal, i.e. that the errors in the observations are not spatially correlated. By contrast, the off-diagonal components of $\boldsymbol{B}$ play an important role in extending information on N_0' in the vertical, as will be described in section 3.4.5.

Unfortunately, the lidar (and to a lesser extent the radar) measurements may be noisy, which can contaminate the retrieved α_v, as shown by Hogan et al. (2006b). Therefore, we add a smoothness constraint to the retrieved extinction, represented by the final term in (7), in which ***T*** is a "Twomey-Tikhov" matrix (Rogers 2000, Ansmann and Muller 2005). This matrix penalizes the second derivative of the lnα_v and ln*S* profiles, resulting in a smoother profile that is able to closely forward model the lidar backscatter without reproducing any of its random measurement noise. ***T*** is of size $(n+m+g) \times (n+m+g)$, and for $n = 6$, the top-left $n \times n$ elements of the matrix (i.e. those that correspond to the α_v elements of x) are given by

$$\boldsymbol{T}_{1..n,1..n} = \kappa \begin{pmatrix} 1 & -2 & 1 & 0 & 0 & 0 \\ -2 & 5 & -4 & 1 & 0 & 0 \\ 1 & -4 & 6 & -4 & 1 & 0 \\ 0 & 1 & -4 & 6 & -4 & 1 \\ 0 & 0 & 1 & -4 & 5 & 2 \\ 0 & 0 & 0 & 1 & -2 & 1 \end{pmatrix}. \quad (8)$$

It may not be immediately obvious to the reader where these numbers come from, but they can be derived by writing the last term of the cost function in (7) as the sum of the square of the finite-difference form of the second derivatives of a column of values in the state vector. So if we have the column vector $\mathbf{x}=[x_1, x_2, \ldots, x_n]$, then this quantity will be $\mathbf{x}^T\mathbf{Tx}/\kappa=(x_1-2x_2+x_3)^2 + (x_2-2x_3+x_4)^2 + \ldots + (x_{n-2}-2x_{n-1}+x_n)^2$. By multiplying out all the squared terms, it can be shown that the matrix **T** has the form given by (8).

Note that if multiple cloud layers are present in the profile then the α_v element corresponding to the lowest level of one cloud layer will be adjacent in the state vector to the element corresponding to the highest level of the cloud layer below. The elements of ***T*** are therefore set independently for each cloud layer, to avoid artificially smoothing between non-adjacent layers. A similar submatrix is used for those parts of ***T*** that correspond to the lidar-ratio profile. Since the smoothing is only applied to these two variables, the other elements of ***T*** are set to zero. The coefficient κ controls the degree of smoothing and in practice needs to be chosen subjectively depending on the magnitude of the random errors in the lidar signal and the vertical resolution. We use a value of 100 for lnα_v.

The cost function cannot be minimized in one step because of the presence of the non-linear forward model operator $H(\boldsymbol{x})$, so we use the Gauss-Newton method [Rodgers (2000)] in which a linearized version of the cost function is minimized iteratively. At iteration k we have an estimate of the state vector, $\boldsymbol{x}_k$, and the corresponding forward-model estimate of the observations, $H(\boldsymbol{x}_k)$. The linearized cost function J_L is obtained by replacing $H(\boldsymbol{x})$ in (7) by $H(\boldsymbol{x}_k)+\boldsymbol{H}\times(\boldsymbol{x}-\boldsymbol{x}_k)$, where ***H*** is the *Jacobian*, a matrix containing the partial derivative of each observation with each respect to each element of the state vector. In this case ***H*** is a $(p+q+2) \times (n+m+g)$ matrix given by

$$
H = \begin{pmatrix}
\frac{\partial \beta_1}{\partial \alpha_{v,1}} & \cdots & \frac{\partial \beta_1}{\partial \alpha_{v,n}} & \frac{\partial \beta_1}{\partial S_1} & \cdots & \frac{\partial \beta_1}{\partial S_g} & \frac{\partial \beta_1}{\partial N_{b,1}} & \cdots & \frac{\partial \beta_1}{\partial N_{b,m}} \\
\vdots & \ddots & \vdots & \vdots & \ddots & \vdots & \vdots & \ddots & \vdots \\
\frac{\partial \beta_p}{\partial \alpha_{v,1}} & \cdots & \frac{\partial \beta_p}{\partial \alpha_{v,n}} & \frac{\partial \beta_p}{\partial S_1} & \cdots & \frac{\partial \beta_p}{\partial S_g} & \frac{\partial \beta_p}{\partial N_{b,1}} & \cdots & \frac{\partial \beta_p}{\partial N_{b,m}} \\
\frac{\partial Z_1}{\partial \alpha_{v,1}} & \cdots & \frac{\partial Z_1}{\partial \alpha_{v,n}} & \frac{\partial Z_1}{\partial S_1} & \cdots & \frac{\partial Z_1}{\partial S_g} & \frac{\partial Z_1}{\partial N_{b,1}} & \cdots & \frac{\partial Z_1}{\partial N_{b,m}} \\
\vdots & \ddots & \vdots & \vdots & \ddots & \vdots & \vdots & \ddots & \vdots \\
\frac{\partial Z_q}{\partial \alpha_{v,1}} & \cdots & \frac{\partial Z_q}{\partial \alpha_{v,n}} & \frac{\partial Z_q}{\partial S_1} & \cdots & \frac{\partial Z_q}{\partial S_g} & \frac{\partial Z_q}{\partial N_{b,1}} & \cdots & \frac{\partial Z_q}{\partial N_{b,m}} \\
\frac{\partial I_\lambda}{\partial \alpha_{v,1}} & \cdots & \frac{\partial I_\lambda}{\partial \alpha_{v,n}} & \frac{\partial I_\lambda}{\partial S_1} & \cdots & \frac{\partial I_\lambda}{\partial S_g} & \frac{\partial I_\lambda}{\partial N_{b,1}} & \cdots & \frac{\partial I_\lambda}{\partial N_{b,m}} \\
\frac{\partial \Delta I}{\partial \alpha_{v,1}} & \cdots & \frac{\partial \Delta I}{\partial \alpha_{v,n}} & \frac{\partial \Delta I}{\partial S_1} & \cdots & \frac{\partial \Delta I}{\partial S_g} & \frac{\partial \Delta I}{\partial N_{b,1}} & \cdots & \frac{\partial \Delta I}{\partial N_{b,m}}
\end{pmatrix}, \tag{9}
$$

and is calculated at the same time as the forward model, as will be described in section 3. In order to improve the readability of $\boldsymbol{H}$, we have not displayed the logarithm of the variables β, Z, α_v, N_b and S, or the primes on any of the forward-modeled variables. The lower two rows are omitted for producing the "DARDAR cloud properties" product.

By setting the derivative of J_L with respect to each element of $\boldsymbol{x}$ to zero and rearranging, an expression for the state vector at the minimum of J_L is obtained:

$$
\boldsymbol{x}_{k+1} = \boldsymbol{x}_k + \boldsymbol{A}^{-1}\left[\boldsymbol{H}^T \boldsymbol{R}^{-1} \delta \boldsymbol{y} - \boldsymbol{B}^{-1}\left(\boldsymbol{x}_k - \boldsymbol{x}^a\right) - \boldsymbol{T}\boldsymbol{x}_k\right], \tag{10}
$$

where the symmetric matrix $\boldsymbol{A}$ is known as the *Hessian* and is given by

$$
\boldsymbol{A} = \boldsymbol{H}^T \boldsymbol{R}^{-1} \boldsymbol{H} + \boldsymbol{B}^{-1} + \boldsymbol{T}. \tag{11}
$$

For efficiency $\boldsymbol{A}$ is not inverted but rather kept on the left hand side of (10) and the matrix problem is solved by Cholesky decomposition, box 12 in Figure 1.

Since we are using an iterative process, a first guess is required for the state vector, $\boldsymbol{x_0}$. For those variables with an *a priori* (N_b and S), the *a priori* value is used, while for α_v, a constant value of 10^{-6} m^{-1} is used. The process is repeated until convergence (box 11 in Figure 1), as determined by a χ^2 convergence test. χ^2 is defined as:

$$
\chi^2 = \sum_{i=1}^{q} \frac{\left(\ln Z_i - \ln Z_i'\right)^2}{\sigma^2_{\ln Z_i}} + \sum_{i=1}^{p} \frac{(\ln \beta_i - \ln \beta_i')^2}{\sigma^2_{\ln \beta_i}} + \frac{\left(I_\lambda - I_\lambda'\right)^2}{\sigma^2_{I_\lambda}} + \frac{\left(\Delta I - \Delta I'\right)^2}{\sigma^2_{\Delta I}} \tag{12}
$$

Or more simply it may be written as $\chi^2 = \boldsymbol{\delta y}^T \boldsymbol{R}^{-1} \boldsymbol{\delta y}$. The iterations are stopped if χ^2 is less than 0.01 or when its value has converged. Convergence is determined to have occurred when the value of χ^2 increases from its value at the previous iteration for the third time. The state vector at the iteration with the minimum value of χ^2 is taken to be the solution. As described earlier, the radar-lidar-radiometer retrieval is performed in two parts: first using only the radar and lidar measurements, and then using this as a first guess of a few more iterations in which the radiance elements are added to the measurement vector. The same convergence criteria are used in each case.

3.4.3 Use of cubic spline basis functions for smoothing N_0'

As mentioned previously, N_0' is represented by a reduced set of *m* basis functions, which ensures a shorter computation time as well as achieving a certain degree of smoothness in the retrieved N_0'. However the forward model described in section 3.4.7 works on the lidar range grid, so at the beginning of each iteration, the *m* amplitudes of the basis functions N_b, within the state vector, have to be converted to *n* values of N_0'. We treat this as a transformation from the state vector $\boldsymbol{x}$ to a high-resolution state vector $\hat{\boldsymbol{x}}$, which is the same as defined in (4) but with the *m* values of N_b replaced by *n* values of N_0'. This step is indicated by box 2 in Figure 1, and is achieved using an $(n+m+g)\times(2n+g)$ matrix $\boldsymbol{W}$:

$$\hat{\boldsymbol{x}} = \boldsymbol{W}\boldsymbol{x} \,. \tag{13}$$

The top-left $(n+g)\times(n+g)$ elements of $\boldsymbol{W}$ correspond to the α_v and *S* elements of $\boldsymbol{x}$ that are unchanged by the transformation, so are represented in $\boldsymbol{W}$ by an identity matrix. The bottom-right $n\times m$ elements of $\boldsymbol{W}$ contain the basis functions. Following Hogan (2007), we use cubic spline basis functions, resulting in the retrieved N_0' being continuous in itself and its first and second derivatives. Details of how to set these elements of $\boldsymbol{W}$ may be found in the appendix of Hogan (2007). The Jacobian that is output from the forward model, $\hat{\boldsymbol{H}}$, is also on the lidar range grid, i.e. it consists of derivatives with respect to N_0' rather the corresponding basis function amplitudes N_b. We convert this high resolution Jacobian to the standard Jacobian used at the basis function resolution by simply post-multiplying by $\boldsymbol{W}$:

$$\boldsymbol{H} = \hat{\boldsymbol{H}}\boldsymbol{W}. \tag{14}$$

3.4.4 Retrieving extinction-to-backscatter ratio

We have 3 different ways to retrieve *S:* assuming *S* is constant, or retrieving *S* varying linearly with temperature. Delanoë and Hogan (2008) assumed that S was constant with height, however this strong constraint can be relaxed when the number of independent measurements allows it, for instance when an independent estimate of αv is available (e.g. from a Raman or high spectral resolution lidar), providing information on the height dependence of S. Unfortunately, CALIPSO does not have such channels, but when infrared radiances are available we have enough independent information to allow S to vary with height in the retrieval. Platt et al. [2002] showed that ln(S) varies linearly with temperature. We assume that the altitude dependence can be used instead of temperature if temperature varies linearly with altitude. In that case, ln(S) is expressed as a linear function of height:

$$\ln(S) = a_{\ln s}(z - z_{mid}) + b_{\ln s}\,, \tag{15}$$

where z is the altitude and z_{mid} the height of the middle of the cloud. Coefficients, $a_{\ln S}$ and $b_{\ln S}$ are, respectively, the slope and the value of ln(S) at the middle of the cloud sampled by the lidar, and they can be used to represent ln(S) in the state vector instead of ln(S). When no radiances are assimilated (e.g. when liquid in the profile prevents the radiance from being forward-modelled using ice properties above), $a_{\ln S}$ is removed from the state vector to revert to the original assumption of Delanoë and Hogan (2008).

3.4.5 Use of a priori error covariances for spreading of number concentration information in height

As described in section 3.4.7.2, an N_0'-temperature relationship is used as an *a priori* constraint on N_0'. Physically, this can be thought of as expressing the fact that lower down in a cloud (i.e. at warmer temperatures), the process of aggregation leads to a smaller number of larger particles. Algorithmically, this ensures that the N_0' retrieved by the scheme tends toward a physical value when only one instrument is available. In the simplest case, the ***B*** matrix is diagonal and the diagonal elements are the error variances of the *a priori* estimate x^a, i.e. $B_{i,i}=\sigma_a^2$ (see Table for the value used).

Very often in spaceborne radar-lidar retrievals, within a single profile we have a region of cloud detected by both radar and lidar, above which is a region detected by lidar alone and below which is a region detected by radar alone. In this case, if ***B*** is diagonal, the retrieved N_0' would be determined closely by the radar and lidar in the region where both detect the cloud, but within the height span of a single basis function, would switch back to a value much closer to the *a priori* in the regions detected by just one instrument.

A more realistic retrieval takes account of the fact that, if in the radar-lidar region the retrieved N_0' is higher than the *a priori* estimate, then we would expect it to be higher in the radar-only and lidar-only regions as well. This tendency is implemented via the off-diagonal elements of ***B***, which express the fact that the difference between the actual value of N_0' and the *a priori* value is spatially correlated. Following Hogan (2007), if we assume that the correlation coefficient between two basis-function coefficients centered at heights z_i and z_j decreases as an inverse exponential with the separation distance, then the off-diagonal covariance terms of ***B*** are given by

$$B_{i,j} = B_{i,i} \exp\left(-\left|z_j - z_i\right| / z_0\right), \tag{16}$$

where z_0 is the decorrelation distance and it has been assumed that σ_a^2 is constant with height.

Table 4: Constants

Variable	Description	Value	Unit
z_0	decorrelation distance	1	km

Note that an *a priori* is used for N_0', so (16) is applied to the N_0' part of ***B***. As yet, there is no observational data to choose a particularly value of z_0, a problem common to many areas of data assimilation Daley (1991).

3.4.6 Calculation of the retrieval error

After the solution has converged, the error covariance matrix, $\boldsymbol{S_x}$, of the retrieved variables held in the state vector is simply given by the inverse of the Hessian matrix (box 13 Figure 1), i.e. $\boldsymbol{S_x} = \boldsymbol{A}^{-1}$ [Rodgers (2000)]. Hence, the first n diagonal terms of $\boldsymbol{S_x}$ represent the error variances in ln α_v, with the remainder representing error variances in ln S and ln N_b. The error covariance matrix of the high-resolution transformation of the state vector $\hat{x}$ defined in (13) is given by pre- and post-multiplying by the weighting function matrix $\boldsymbol{W}$:

$$\hat{\boldsymbol{S}}_x = \boldsymbol{W}\boldsymbol{S}_x\boldsymbol{W}^T. \tag{18}$$

The final n diagonal elements of $\hat{\boldsymbol{S}}_x$ represent the error variances of N_0' at the same resolution as α_v. Errors in any other microphysical variables derived from α_v and N_0' (in particular *IWC* and r_e) may be calculated from $\hat{\boldsymbol{S}}_x$, as described in section 3.4.8

It should be stressed that the retrieval errors obtained in this way depend strongly on the observational errors that are assigned in (6). For the retrieval error to be realistic it is important that the observational errors include the error in the forward model. Formally we may write that the observation error covariance matrix is given by $\boldsymbol{R}=\boldsymbol{O}+\boldsymbol{M}$, where $\boldsymbol{O}$ is the error covariance solely due to instrumental error and $\boldsymbol{M}$ is the forward model error. Discussion of the error associated with each component of the forward model is given in section 3.4.7.4.

3.4.7 Forward model

In this section, the forward model $H(\boldsymbol{x})$ used in the scheme is described. As stated before, the forward model produces an estimate of the observations $\boldsymbol{y}$ from the state vector $\boldsymbol{x}$, and is represented in Figure 1 by the dot-dashed box. In addition to the information held within the state vector, ancillary information is required for each of the components of the forward model. This includes the thermodynamic state of the atmosphere (in particular, profiles of temperature, pressure, humidity and ozone concentration), the properties of the surface (skin temperature and emissivity at the radiometer wavelengths), as well as the properties of the instruments themselves (in particular the lidar field-of-view to calculate the contribution from multiple scattering). Such information can be obtained with adequate accuracy from standard analysis and forecast products.

3.4.7.1 The normalized concentration parameter N_0^* and the look-up tables

Nearly all components of the forward model require the ability to predict arbitrary intensive and extensive variables from the combination of α_v and N_0'. This is achieved by first calculating N_0^* using (3), then using one-dimensional look-up tables to relate the ratio α_v/ N_0^* to either an intensive variable y, or to Y/ N_0^*, where Y is an extensive variable. In this section it will be shown how these look-up tables are generated.

First, we need to decide on a *microphysical model,* describing the shape of the particle size distribution and the relationships between particle mass, cross-sectional area and size. The distributions are formulated in terms of the maximum particle dimension, D. The ice particle mass is assumed to follow the Brown and Francis (1995) density-D relationship when D ≥ 300 micron:

$$\rho(D) = 0.0056D^{-1.1}, \tag{19}$$

where D is in cm and $\rho(D)$ in g cm^{-3}, which was found by Hogan et al. (2006a), to be accurate when calculating Z from aircraft data in mid-latitude ice clouds. The density assumption is encapsulated in the relationships in the look-up table, and so can be changed by recreating the look-up tables with a different assumption. The corresponding area-size relationship when D ≥ 300 micron:

$$A(D) = 0.15189D^{1.64}, \tag{20}$$

where D is in cm and $A(D)$ in cm^2, is taken from Francis et al. (1998), who used the same aircraft dataset as Brown and Francis (1995). When D < 300 micron, we are usung the area-density-diameter relationships of Michtell (1996) for Hexagonal columns. Note that density and area are set to those for solid ice spheres for small D when the implied density from (19) exceeds that for solid ice (0.92 g cm^{-3}).

Adopting the formalism of Delanoë et al. (2005), we describe the size distribution as

$$N(D) = N_0^* F(D / D_0^*), \tag{21}$$

where N_0* is the normalized number concentration parameter, given by

$$N_0^* = \frac{4^4}{\Gamma(4)} M_3^5 / M_4^4, \tag{22}$$

and M_n is the n^{th} moment of the ice particle size distribution (the superscripts represent powers of 4 and 5 in the normal way). Particle size in (21) is normalized by D_0*, a measure of the mean size of the distribution and defined as

$$D_0^* = M_4 / M_3. \tag{23}$$

The function F in (21) is the "unified" size distribution shape given by Delanoë et al. (2005), and has been found to fit measured size distributions when they are appropriately normalized (i.e. F fits N / N_0* versus D / D_0^*).

To generate the look-up tables, we cycle through a wide range of values of D_0^* and for each calculate α_v / N_0*, y and Y / N_0* (where y and Y represent all intensive and extensive variables of interest). Geometric optics is used to calculate α_v via the area-size relationship discussed above. In the case when Y represents radar reflectivity factor Z, Mie theory is applied assuming the particles to be homogeneous ice-air spheres of diameter D and mass m. Similarly, the ice water content, IWC, is simply the integrated particle mass across the size distribution. The intensive variable effective radius, r_e, is derived using Foot (1988):

$$r_e = \frac{3}{2} \frac{\mathrm{IWC}}{\alpha_v \rho_i}, \tag{24}$$

where ρ_i is the density of solid ice. Other variables are derived in a similar fashion, as detailed in Table 3

Table 3: lookup tables

Variable	Derived from	Comments	Used for

Variable	Derived from	Comments	Used for
r_e	α_v / N_0*	Effective radius: directly retrieved	Cloud parameter
IWC	α_v / N_0*	First we retrieve IWC/ N_0*, then using N_0* we derive IWC	Cloud parameter
r_a	α_v / N_0*	Mean equivalent-area radius	Lidar model
Z	α_v / N_0*	We use Mie theory (radar at 94GHz) to derive Z/ N_0*. First we calculate Z/ N_0*, then using N_0* we derive Z	Radar model
$\alpha_{8.55}$	α_v / N_0*	We use Mie theory to derive the extinction coefficient at 8.55 microns for size distributions described in the text, and store the results in the form of a look-up table of $\alpha_{8.55}$/ N_0* versus α_v/ N_0*. In the algorithm we then using α_v / N_0* from the state vector to calculate $\alpha_{8.55}$/ N_0*, then using N_0* we derive $\alpha_{8.55}$.	Radiative model
α_{11}	α_v / N_0*	We use Mie theory to derive the extinction at 11 um. Using α_v / N_0* we calculate α_{11}/ N_0*, then using N_0* we derive α_{11}	Radiative model
α_{12}	α_v / N_0*	We use Mie theory to derive the extinction at 12 um. Using α_v / N_0* we calculate α_{12}/ N_0*, then using N_0* we derive α_{12}	Radiative model
$\tilde{w}_{8.55}$	α_v / N_0*	We use Mie theory to derive the single-scatter albedo at 8.55 um. In the algorithm we use α_v/ N_0* to calculate $\tilde{w}_{8.55}$.	Radiative model
$\tilde{w}_{11}$	α_v / N_0*	We use Mie theory to derive the single-scatter albedo at 11 um. Using α_v / N_0* we calculate $\tilde{w}_{11}$.	Radiative model
$\tilde{w}_{12}$	α_v / N_0*	We use Mie theory to derive the single-scatter albedo at 12 um. Using α_v / N_0* we calculate $\tilde{w}_{12}$.	Radiative model
$g_{8.55}$	α_v / N_0*	We use Mie theory to derive the asymmetry factor at 8.55 um. Using α_v / N_0* we calculate $g_{8.55}$	Radiative model

Variable	Derived from	Comments	Used for
g_{11}	α_v / N_0*	We use Mie theory to derive the asymmetry factor at 11 um. Using α_v / N_0* we calculate g_{11}	Radiative model
g_{12}	α_v / N_0*	We use Mie theory to derive the asymmetry factor at 12 um. Using α_v / N_0* we calculate g_{12}	Radiative model

To demonstrate this approach, Figure 2 (a) shows α_v as a function of 94-GHz Z derived from the same large *in situ* aircraft database used by Delanoë et al. (2005) and Protat et al. (2007). There is clearly no unique relationship between the two variables, but Figure 2 shows that when both are normalized by N_0*, the points collapse on to a much tighter curve. These observations are well fitted by the gray line, which indicates the look-up table derived using using the unified size distribution shape discussed above. The same behavior is exhibited for all other extensive variables.

Hence this can be used to predict Z and an other microphysical variables required in the forward model from the combination of α_v and N_0* using one-dimensional look-up tables. In principle, any other pair of moments could be used to generate the required variables, but if one of them was not N_0* then the lookup tables would have to be two-dimensional.

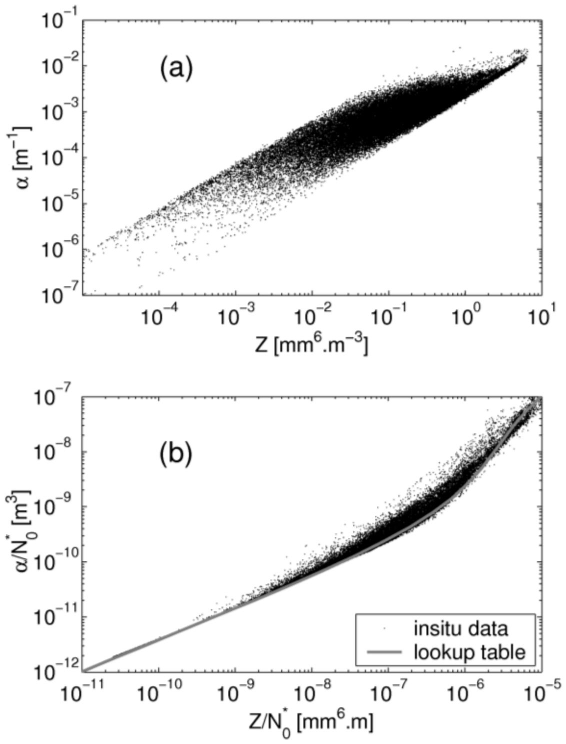

Figure 2: (a) Visible extinction coefficient av as a function of 94-GHz radar reflectivity factor Z for the large in situ aircraft database of Delanoë et al. (2005). (b) The same but after dividing both variables by the normalized number concentration parameter N0*. The gray line corresponds to the fit calculated using the unified size distribution shape. The curved shape in the relationship is due to the transition between Rayleigh scattering at small particle sizes to Mie scattering at larger sizes.

3.4.7.2 A priori of the normalized concentration parameter N_0^*

As discussed in section 3.4.1, a desirable property of at least one of the state variables is that we have a good *a priori* estimate of it from temperature (*T*), in order that when only the radar or the lidar are available, the retrieval is at least as accurate as existing empirical relationships based on temperature in the literature (e.g. Hogan et al. 2006a).

Figure (a) shows the temperature dependence of N_0^* using the same *in situ* database as used in, Figure 2. It can be seen that, although there is such a relationship, it is not IWC independent. For both this reason, and in order to reduce the scatter, we divide it by a power of the visible extinction coefficient.

A range of powers has been tested and it is found that the best results are found for a power of 0.61; Figure (b) clearly shows that there is an IWC-independent relationship between $N_0^*/\alpha_v^{0.61}$ and temperature. Hereafter this ratio will be represented by N_0'. Because a good *a priori* is available for N_0', it is used in the state vector rather than N_0^*, but N_0^* needs to still be calculated as the first step in the forward model (box 2 in Figure 1) before all the other variables can be calculated. The spread of the points in Fig. 3b indicates that ln N_0' has a variance of 1.0 (Table), so this is the value used for the *a priori* error variance $B_{i,j}$ discussed in section 3.3.5.

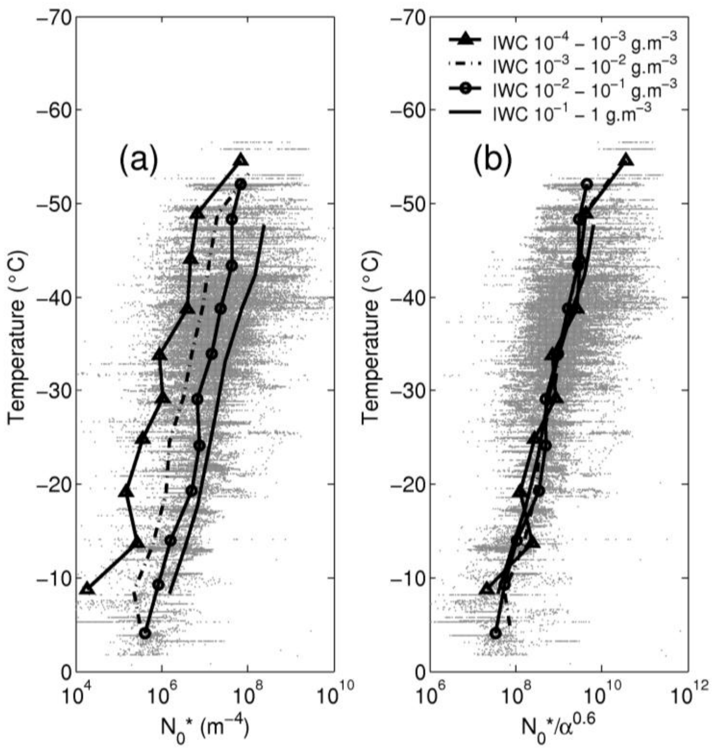

Figure 3: (a) The temperature dependence of N_0* for each size distribution within the large in situ database of Delanoë et al. (2005) (dots), superimposed by the mean N_0* in 5 ° C temperature ranges and various ranges of ice water content IWC (lines and symbols). (b) The same but for the variable $N_0' = N_0^*/\alpha_v^{0.61}$

3.4.7.3 Radar forward model

The look-up tables calculated in section 3.4.7.1 are used in the forward model to derive *Z* from α_v and N_0*, using the relationship between Z / N_0* and α_v / N_0* shown in Fig. 2, and represented by box 3 in Figure 1. Gaseous attenuation at the radar wavelength is calculated using the look-up tables generated from the line-by-line model of Liebe (1985), coupled to estimated profiles of temperature, pressure and humidity as part of the ancillary data if it has not been already done in the merged file. Note that Liebe (1985) may not still be state-of-the-art, but it would be straightforward to use an alternative model. Ice attenuation is believed to be small enough to be neglected (e.g. Hogan and Illingworth 1999, although they specifically considered 79 GHz which is very close to 94 GHz in terms of the extinction due to ice particles). Note that it would be straightforward to relax this assumption by including attenuation in the radar forward model.

The Jacobian of the radar forward model, i.e. the partial derivatives of ln *Z* at each gate with respect to ln α_v and ln N_0', may be calculated efficiently using the gradient of the relevant look-up tables.

The second part of the radar forward model is the calculation of the part of the high resolution Jacobian $\hat{\boldsymbol{H}}$ (mentioned in section 3.4.3) that contains the partial derivatives of ln *Z* with respect to each element of the state vector ***x***. This is represented (for all instruments) by box 9 in Figure 1. The derivative of ln *Z* at high-resolution gate *i* with respect to the logarithm α_v at gate *i*, keeping N_0* constant, is:

$$\left.\frac{\partial \ln Z_i}{\partial \ln \alpha_{v,i}}\right|_{N_0^*} = \frac{\partial \ln(Z_i / N_{0,i}^*)}{\partial \ln(\alpha_{v,i} / N_{0,i}^*)}. \tag{25}$$

The derivative $\partial \ln(Z_i / N_{0,i}^*) / \partial \ln(\alpha_{v,i} / N_{0,i}^*)$ is derived directly from the lookup-table by computing the slope of the relationship between the logarithms of Z / N_0* and α_v / N_0*. If we neglect attenuation in ice cloud then *Z* at gate *i* does not depend on α_v at any other gate *j*, so

$$\left.\frac{\partial \ln Z_{i\neq j}}{\partial \ln \alpha_{v,j}}\right|_{N_0^*} = 0. \tag{26}$$

The partial derivative with respect to N_0' is derived in a similar fashion

$$\left.\frac{\partial \ln Z_i}{\partial \ln N_{0,i}'}\right|_{\alpha_v} = \left.\frac{\partial \ln Z_i}{\partial \ln N_{0,i}^*}\right|_{\alpha_v} = 1 - \frac{\partial \ln(Z_i / N_{0,i}^*)}{\partial \ln(\alpha_{v,i} / N_{0,i}^*)}, \tag{27}$$

while the off-diagonal terms are again zero:

$$\left.\frac{\partial \ln Z_{i\neq j}}{\partial \ln N_{0,j}^*}\right|_{\alpha_v} = 0. \tag{28}$$

Since the reflectivity factor is totally independent of the lidar extinction-to-backscatter ratio *S*, the partial derivative with respect to *S* is equal to zero.

3.4.7.4 *Forward model error*

As discussed in section 3.4.6, it is important to include the contribution of forward-model error to the observation error covariance matrix **R**. In the case of the radar model, the leading source of error is due to the representation of the size distribution by a unique modified gamma shape (see 3.4.7.1 for more details). The spread of points in the *in situ* microphysical data set cannot be represented in the lookup tables, which contributes to a root-mean-squared random error in *Z.* Additional errors are associated with the approximation of ice particles by homogeneous ice-air spheres, which is required for Mie theory to be applied. This approximation leads us to assume a density-diameter relationship, which is used to calculate the ice fraction of the homogeneous ice-air spheres. We consider a random error in Z due to microphysical assumptions (particle size distribution and density) of ΔZ_{micro}= 1 dB. This comes from a combination of the spread of points in the x-direction in Fig. 2b (the contribution from uncertainty in the particle size distribution), and from the degree of agreement found between aircraft and radar scans by Hogan et al. (2006a) (the contribution from uncertainty in the density). Forward lidar model error is mainly due to the error in extinction-to-backscatter ratio and multiple scattering effects so we assign an error of 0.3 to $\ln\beta$, although it is admitted that this value is somewhat arbitrary and may need to be revised in light of future work.

Table 6: Forward model error values

Variable	Value	Unit
Z_{error}	1	dB
$\ln \beta_{error}$	0.3	none

The error in the forward modelled radiance is little more complicated, since it depends on cloud thickness, surface temperature and error in meteorological parameters such as the temperature profile. The infrared radiance forward model used here is described in section 3.5.2 (and more detailed in Delanoë and Hogan, 2008), where each individual radiance calculations employs the “two-stream source function technique”. Comparisons with the 16-stream DISORT code demonstrated that for zenith radiances our code is accurate to better than 1% (see Delanoë and Hogan 2008), thereby justifying the use of only two streams. However this study did not include uncertainties in the input parameters. In the literature, different sources of uncertainties have been explored, including the error in modelling infrared radiances I_λ and the radiance difference ΔI due to different particle habit assumptions and errors in humidity and ozone profiles. However these errors are negligible compared to errors due to other input parameters; skin temperature, emissivity and temperature errors.

Skin temperature and emissivity errors have an effect on observed top-of-atmosphere radiances that is dependent on the optical depth of the intervening cloud, and consequently need to be considered carefully. Our radiative model uses a two-stream calculation to estimate the upwelling and downwelling monochromatic fluxes $F^{\pm}$, which are then used as the source function in a radiance calculation for the radiance measured by the MSI. Unfortunately, this model is too complicated to rigorously work out the radiance error associated with a particular skin temperature error. Therefore, a much simpler model of infrared radiative transfer is assumed for the purpose of calculating error propagation, although we stress that in the subsequent forward modelling of radiances, the full two-stream model is used.

For estimating the first-order contributions of the surface and the cloud to the measured radiance, it is valid to neglect scattering (which is weak in the infrared) and gaseous absorption (which is weak in the window region of the spectrum); therefore, assuming a single layer of physically thin cloud overlying a surface with an emissivity of unity, we may write the radiance measured by MSI as

$$I_\lambda = \varepsilon_c B(T_c)/\pi + (1-\varepsilon_c) B(T_s)/\pi, \tag{29}$$

where ε_c is the emissivity of the cloud, B is the Planck function, and T_c and T_s are respectively cloud and surface temperatures. Of course, (29) is not accurate enough to use as a complete forward model, but since errors only need to be estimated to one significant figure, it is sufficiently accurate to estiamate errors, which is our purpose here. For a radiance in the zenith direction, cloud emissivity can be estimated from the infrared absorption optical depth (τ_λ):

$$\varepsilon_c = 1 - \exp(-\tau_\lambda)\,. \tag{30}$$

Infrared optical depth can be well approximated as the half of visible optical depth and the cloud emissivity becomes:

$$\varepsilon_c = 1 - \exp(-\tau_v/2)\,. \tag{31}$$

Since the radiances are only introduced into the retrieval after the radar-lidar part of the algorithm has been run to convergence, we may use the visible optical depth derived by radar-lidar here. In practice it is found that the radar and lidar provide an optical depth that is close to the value using all three instruments, and therefore the use of this optical depth does not introduce substantial uncertainty in the calculation of the error in I_λ.

We take the partial derivative of (29) with respect to ε_c, T_c and T_s, and by assuming each error is independent may sum the squares of the results to obtain the error variance of the radiance:

$$\begin{aligned} \Delta I_\lambda^2 &= \Delta\varepsilon_c^2 \left[B(T_c) - B(T_c)\right]^2/\pi^2 \\ &+ \Delta T_c^2 \varepsilon_c^2 \left[dB(T_c)/dT_c\right]^2/\pi^2 \\ &+ \Delta T_s^2 (1-\varepsilon_c)^2 \left[dB(T_s)/dT_s\right]^2/\pi^2 \end{aligned} \tag{32}$$

where ΔT_s is the error in surface temperature, which is assumed 3 K for ECMWF forecasts according to Morcrette (2001). ΔT_c is the error in cloud temperature; we use a value of 0.6 K, which was the estimated error of ECMWF temperature forecasts by Benedetti (2005). This value does seem rather low, but unfortunately the Benedetti (2005) reference is the only one that we have been able to get hold of. Certainly it would be straightforward to change the assumption in light of future work and communication with ECMWF. An additional consideration is that we require the temperature at a 1-km horizontal scale, but the ECMWF value will be the average over a 25-km model gridbox. Note that if this number is increased from the current value of 0.6 K, then it means that the infrared radiance will contribute proportionately less to the retrieval. Future work ought to include a sensitivity test to investigate the impact of errors in temperature in interpretting infrared radiances. If the errors are genuinely large, then including infrared radiances in a retrieval will only have the effect of degrading it. The final point to note is that the ECMWF temperatures will be provided on a pressure grid, and there will be a small amount of error in interpolation due to the model's pressure error. However, this is believed to be less than the absolute temperature error.

The gradients of the Planck function are straightforward to calculate at the temperature of the surface and the temperature of the cloud (taken to be the cloud-top temperature as detected by the lidar). The random error in cloud emissivity, $\Delta\varepsilon_c$, could be derived from visible optical depth, but it needs to be remembered that we are calculating the error in radiance *due to parameters in the forward model that are held constant during the subsequent retrieval process*. Since the cloud optical depth, and hence the cloud emissivity, will be varied in order to better match the observed radiance in the subsequent retrieval, this component of the error in (32) is set to zero.

It is clear that the errors in radiance will be strongly dependent on the visible optical depth retrieved in the first part of the algorithm: optically thin clouds will let through a substantial amount of radiation from the surface, and therefore the surface temperature error contributes significantly to the error in the radiance forward model. For optically thick clouds, ε_c is close to unity, almost all the measured radiation was emitted by the cloud, and hence the errors in forward modelling the radiance arise entirely from the error in the temperature profile. Errors in ΔI are estimated by combining the errors for the two contributing radiances.

3.4.8 Computing the retrieval error in ice water content and effective radius

As outlined in section 3.4.6, $\boldsymbol{S_x}$ contains the error variances and covariances of the retrieved ln α_v, ln S and ln N_0', with ln α_v and ln N_0' both having n elements. In this section we describe how the errors and error covariances in *IWC* and r_e may be derived rigorously and in a way that may be easily extended to any other extensive or intensive variable. Note that all calculations here are done with the matrices transformed such that all variables are held on the high resolution grid of the observations, rather than being in the form of basis function coefficients. However, for simplicity the "hats" used in section 3.4.6 have been omitted from $\boldsymbol{S_x}$ and $\boldsymbol{x}$.

Defining column vector $\boldsymbol{m}$ as:

$$\boldsymbol{m} = \begin{pmatrix} \ln \mathrm{IWC}_1 \\ \vdots \\ \ln \mathrm{IWC}_n \\ r_{e,1} \\ \vdots \\ r_{e,n} \end{pmatrix}, \qquad (33)$$

the task is to compute the corresponding error covariance matrix, $\boldsymbol{S_m}$. As described in section 3.4.7.1, the look-up tables can provide any variable in terms of N_0^* and the ratio α_v / N_0^*. It is therefore convenient to consider an intermediate column vector $\boldsymbol{u}$ that contains these entities:

$$
\boldsymbol{u} = \begin{bmatrix} \ln(\alpha_{v,1} / N^*_{0,1}) \\ \vdots \\ \ln(\alpha_{v,n} / N^*_{0,n}) \\ \ln N^*_{0,1} \\ \vdots \\ \ln N^*_{0,n} \end{bmatrix} \tag{34}
$$

This may be obtained from $\boldsymbol{x}$ using $\boldsymbol{u} = \boldsymbol{Ux}$, where the matrix $\boldsymbol{U}$ describes how the elements of $\boldsymbol{x}$ are transformed to the elements of $\boldsymbol{u}$. From (3) we derive $\ln N^*_0 = \ln N_0{}' + 0.61 \ln \alpha_v$ and $\ln(\alpha_v / N^*_0) = 0.39 \ln \alpha_v - \ln N_0{}'$. Therefore, for the case of n = 2 and for S represented by a single number, the matrix $\boldsymbol{U}$ would be

$$
\boldsymbol{U} = \begin{pmatrix} 0.4 & 0 & 0 & -1 & 0 \\ 0 & 0.4 & 0 & 0 & -1 \\ 0.6 & 0 & 0 & 1 & 0 \\ 0 & 0.6 & 0 & 0 & 1 \end{pmatrix}, \tag{35}
$$

where the column of zeros in the middle corresponds to the central element of $\boldsymbol{x}$ that contains ln *S*; this is not represented in $\boldsymbol{u}$. Following (18), the error covariance matrix for $\boldsymbol{u}$ is given by $\boldsymbol{S}_u = \boldsymbol{US}_x\boldsymbol{U}^T$. The last step is to define the matrix $\boldsymbol{M}$ such that we can write $\boldsymbol{S}_m = \boldsymbol{MS}_u\boldsymbol{M}^T$. This matrix is similar to a Jacobian in the sense that it contains the partial derivatives of each element of $\boldsymbol{m}$ with respect to each element of $\boldsymbol{u}$. The look-up tables are of the form $\mathrm{IWC} / N^*_0 = f_{\mathrm{IWC}}\left(\alpha_v / N^*_0\right)$, or equivalently $\ln \mathrm{IWC} = \ln N^*_0 + \ln f_{\mathrm{IWC}}\left(\alpha_v / N^*_0\right)$, where f_{IWC} represents the look-up table for IWC. Hence for n = 2 we have

$$
M = \begin{bmatrix} \frac{\partial \ln(\mathrm{IWC}_1 / N^*_{0,1})}{\partial \ln(\alpha_{v,1} / N^*_{0,1})} & 0 & 1 & 0 \\ 0 & \frac{\partial \ln(\mathrm{IWC}_2 / N^*_{0,2})}{\partial \ln(\alpha_{v,2} / N^*_{0,2})} & 0 & 1 \\ \frac{\partial r_{e,1}}{\partial \ln(\alpha_{v,1} / N^*_{0,1})} & 0 & 0 & 0 \\ 0 & \frac{\partial r_{e,2}}{\partial \ln(\alpha_{v,2} / N^*_{0,2})} & 0 & 0 \end{bmatrix}, \tag{36}
$$

where the partial derivatives are simply the gradients of the look-up tables. Bringing the preceding analysis together, the error covariance of $\boldsymbol{m}$ may be derived directly from the error covariance of the state vector using $\boldsymbol{S}_m = \boldsymbol{MUWS}_x\boldsymbol{W}^T\boldsymbol{U}^T\boldsymbol{M}^T$.

3.4.9 Miscellaneous

In deep convective clouds observed by spaceborne radar, it has been shown that multiple scattering can be important [Battaglia et al. (2007)]. In such situations, a number of the assumptions made in this retrieval scheme would become inappropriate, particularly the use of the Brown and Francis (1995) mass-size relationship, which is suitable for low-density aggregates. However, in principle a fast radar multiple scattering model, such as the one of Hogan and Battaglia (2007), could be incorporated. At present a fast method to calculate the Jacobian is not available for this model.

Another source of error arises due to the mismatch of the radar and lidar beams. Illingworth et al. (2000) investigated this effect, and they estimated an error of 0.1 dB when the lidar samples through the middle of the radar footprint, increasing to 0.7 dB for a separation of radar and lidar footprints of 1 km. These values correspond to the RMS difference in reflectivity that would be found if the lidar measured the same quantity as the radar. Accordingly, we usually consider data to be acceptable when the separation distance is less than 1 km, otherwise the alignment cannot be trusted and no retrieval is performed. Fortunately, in 97% of the time this distance does not exceed 1 km.

3.5 External models

3.5.1 Lidar multiple-scattering forward model (Hogan 2006)

To include molecular scattering and multiple scattering, we use the fast multiple-scattering model of Hogan (2006), which has been found to be as accurate as the widely-used Eloranta (1998) model when taken to 5th order scattering, but is over 3 orders of magnitude faster for a 50-point profile. The model is represented by box 6 of Figure 1 and takes as input the lidar ratio *S*, profiles of α_v and the "equivalent-area radius" r_a, i.e. the radius of a sphere with the same cross-sectional area as the mean area of the entire size distribution. A look-up table is used to convert α_v / N_0* to r_a (box 5 of Figure 1).

In order to estimate the molecular return, the profile of atmospheric density is required. The model produces an estimate of the profile of apparent backscatter, as well as the top-left *p* × *n* part of the Jacobian *H* in (9) that contains $\partial \ln \beta_i / \partial \ln \alpha_{v,j}$. An alternative faster method to calculate the Jacobian was provided by Hogan (2008). Note that $\partial \ln \beta_i / \partial \ln \alpha_{v,j}$ is lower-triangular in the sense that β_i only depends on values of $\alpha_{v,i}$ earlier in the profile, so values corresponding to $j > i$ are zero.

We also require the elements of the Jacobian corresponding to the other terms in the state vector. The Jacobian with respect to the cloud extinction-to-backscatter ratio *S* is expressed as $\partial \ln \beta_i / \partial \ln S = -1$.

The Jacobian with respect to N_0* arises due to the particle-size dependence of multiple scattering. Since this is relatively weak, we assume for both channels (Mie and Rayleigh) that

$$\left.\frac{\partial \ln \beta}{\partial \ln N_0^*}\right|_{\alpha_v} = 0, \qquad (37)$$

due to the fact that in practice β is primarily dependent on α_v and only weakly dependent on particle size and N_0*.

Regarding the partial derivative of β with respect to the visible extinction parameter, the upper diagonal is always equal to zero since the lidar signal at i^{th} gate is not affected by the further i+1^{th} gate:

$$\left.\frac{\partial \ln \beta_i}{\partial \ln \alpha_{v\,j>i}}\right|_{N_0^*} = 0\,. \tag{38}$$

The lidar model gives us $\left.\frac{\partial \ln \beta_i}{\partial \ln \alpha_{v\,j<i}}\right|_{N_0^*}$ and $\left.\frac{\partial \ln \beta_i}{\partial \ln \alpha_{v\,i}}\right|_{N_0^*}$ as described in Delanoe and Hogan (2008).

3.5.2 Infrared radiance forward model

For each infrared radiometer channel, the radiance forward model takes as input the relevant cloud variables from the state vector (profiles of visible extinction coefficient α_v and N_0') and estimates of other variables (profiles of temperature, pressure, humidity, O_3 and CO_2 concentrations, as well as skin temperature and emissivity). It produces an estimate of the radiance measured by the instrument as well as the Jacobian with respect to each of the cloud variables from the state vector.

The scattering and absorption properties of ice are taken from the database of Baran (2003), which assumes aggregates. At each radiometer wavelength λ, the ice particle distributions described in section 3.4.7.1 have been used to create look-up tables such that from an input profile of α_v and N_0*, profiles can be calculated of extinction coefficient α_λ, single-scatter albedo $\tilde{w}_\lambda$ and asymmetry factor g_λ. This is illustrated by box 7 of Figure 1.

The forward model was described more fully by Delanoë and Hogan (2008), and therefore, as it is treated as an external module, only a brief overview will be provided here. Gaseous absorption is represented using the correlated-k-distribution method similar to that described by Fu and Liou (1993); the radiance code is essentially run multiple times to represent the variation of absorption coefficient within the wavelength band of a particular channel. Line-by-line calculations using the code of Kato et al. (1999) have been performed to determine the number of quadrature points required and to produce the necessary look-up tables for each satellite channel of interest. The spectral features of different gases within a channel are assumed to overlap randomly, i.e. the wavelengths of the peaks and troughs in the absorption spectrum of one gas are uncorrelated to the wavelengths of the peaks and troughs for the other gases. For example, for the MODIS channel 29 at 8.55 μm, numerical integration over the spectral region requires 9 quadrature points for the H_2O absorption spectrum and 2 quadrature points for the O_3 spectrum, resulting in 18 independent radiative transfer calculations. The cloud properties are kept constant in each calculation. The final radiance and Jacobian are computed as a weighted average of the radiances and Jacobians from each individual calculation, using Gaussian Quadrature.

The individual radiance calculations employ the "two-stream source function technique" of Toon et al. (1989), which is very fast but still represents scattering with sufficient accuracy to be used in the infrared when clouds are present. This is illustrated by box 8 in Figure 1. The method used here is described in Delanoe and Hogan (2008). The radiance model takes as inputs the variables $\alpha_{8.55}$, α_{11}, α_{12}, $\tilde{w}_{8.55}$, $\tilde{w}_{11}$, $\tilde{w}_{12}$, $g_{8.55}$, g_{11} and g_{12} (although in practice only two wavelengths are used, by default 11 and 12 μm) deduced from visible extinction and N_0*. The model computes the infrared radiances at 8.55, 11 and 12 nm and for the Jacobian $dI_\lambda/d\alpha_v$ and dI_λ/dN_0^*.

Monochromatic calculations with the infrared radiance forward model have been validated against DISORT (reported by Delanoe and Hogan 2008), verifying that the “two-stream source function” approach is appropriate.

REFERENCES

Keyword	Reference
Ansmann and Müller (2005)	Ansmann, A., and D. Müller (2005), Lidar and atmospheric aerosol particles, in *Lidar range-resolved optical remote sensing of the atmosphere*, edited by C. Weitkamp, Springer.
Battaglia et al. (2007)	Battaglia, A., M. O. Ajewole, and C. Simmer (2007), Evaluation of radar multiple scattering effects in Cloudsat configuration, *Atmos. Chem. Phys.*, *7*, 1719--1730.
Benedetti (2005)	Benedetti, A. CloudSat AN-ECMWF ancillary data interface control document. 2005. Technical document, CloudSat Data Processing Cent., Fort Collins, Colo., 16 July. (Available at http://cloudsat.cira.colostate.edu/ICD/AN-ECMWF/AN-ECMWF_doc_v4.pdf).
Brown and Francis (1995)	Brown, P. R. A., and P. N. Francis (1995), Improved measurements of the ice water content in cirrus using a total-water probe, *J. Atmos Oceanic. Technol.*, *12*, 410-414.
Brown et al. (1995)	Brown, P. R. A., A. J. Illingworth, A. J. Heymsfield, G. M. McFarquhar, K. A. Browning and M. Gosset, 1995: The role of spaceborne millimeter-wave radar in the global monitoring of ice cloud. J. Appl. Meteorol., 34, 2346-2366.
Cadet et al.(2005)	Cadet, B., V. Giraud, M. Haeffelin, P. Keckhut, A. Rechou, and S. Baldy (2005), Improved retrievals of the optical properties of cirrus clouds by a combination of lidar methods, *Appl. Opt.*, *44*, 1726--1734.
Cooper et al. (2003)	Cooper, S. J., T. S. L'Ecuyer, and G. L. Stephens (2003), The impact of explicit cloud boundary information on ice cloud microphysical property retrievals from infrared radiances, *J. Geophys. Res.*, *108*, 4107--4123.
Chen et al. (2002)	Chen, W.-N., C.-W. Chiang, and J.-B. Nee (2002), Lidar ratio and depolarization ratio for cirrus clouds, *Appl. Opt.*, *41*, 6470--6476.
Chiriaco et al. (2004)	Chiriaco, M., H. Chepfer, V. Noel, A. Delaval, M. Haeffelin, P. Dubuisson, and P. Yang (2004), Improving retrievals of cirrus cloud particle size coupling lidar and three-channel radiometric techniques, *Mon Weath. Rev.*, *132*, 1684--1700.

Keyword	Reference
Delanoë et al. (2005)	Delanoë, J., A. Protat, J. Testud, D. Bouniol, A. J. Heymsfield, A. Bansemer, P. R. A. Brown, and R. M. Forbes (2005), Statistical properties of the normalized ice particle size distribution, *J. Geophys. Res.*, *110*, 10201, doi:10.1029/2004JD005405 .
Delanoë and Hogan (2008)	Delanoë, J., and R. J. Hogan (2008), A variational scheme for retrieving ice cloud properties from combined radar, lidar, and infrared radiometer, *J. Geophys. Res.*, *113*, D07204, doi:10.1029/2007JD009000.
Delanoë and Hogan (2010)	Delanoë , J. and R. J. Hogan (2010), Combined CloudSat-CALIPSO-MODIS retrievals of the properties of ice clouds, J. Geophys. Res., 115, D00H29, doi:10.1029/2009JD012346.
Daley (1991)	Daley, R. (1991), *Atmospheric data analysis*, 457 pp., Cambridge.
Donovan et al. (2001)	Donovan, D. P., A. C. A. P. van Lammeren, H. W. J. Russchenberg, A. Apituley, R. J. Hogan, P. N. Francis, J. Testud, J. Pelon, M. Quante, and J. W. F. Goddard (2001), Cloud effective particles size and water content profile retrievals using ombined radar and lidar observations - 2. Comparison with IR radiometer and in-situ measurements of ice clouds, *J. Geophys. Res.*, *106*, 27,449--27,464.
Eloranta, E. W. (1998)	Eloranta, E. W. (1998), A practical model for the calculation of multiply scattered lidar returns, *Appl. Optics*, *37*, 2464--2472.
McClatchey et al. (1972)	McClatchey, R. A., R. W. Fenn, J. E. A. Selby, F. E. Volz, and J. S. Garing (1972), Optical properties of the atmosphere (3rd ed.), *Air Force Cambridge Research Laboratories*, Rep. No. AFCRL72-0497, L. G. Hanscom Field.
Foot (1988)	Foot, J. S. (1988), Some observations of the optical properties of clouds - 2. Cirrus, *Quart. J. Roy Meteorol. Soc.*, *114*, 145--1647.
Francis et al. (1998)	Francis, P. N., P. Hignett, and A. Macke (1998), The retrieval of cirrus cloud properties from aircraft multi-spectral reflectance measurements during EUCREX'93, *Quart. J. Roy Meteorol. Soc.*, *124*, 1273-1291.
Fu and Liou (1993)	Fu, Q., and K. N. Liou (1993), Parameterization of the radiative properties of cirrus clouds, *J. Atmos. Sci., 50,* 2008– 2025.
Hogan (2006)	Hogan, R. J. (2006): Fast approximate calculation of multiply scattered lidar returns. *Applied Optics, 45,* 5984-5992.
Hogan (2007)	Hogan, R. J., (2007): A variational scheme for retrieving rainfall rate and hail reflectivity fraction from polarization radar. *J. Appl. Meteorol. Climatology, 46,* 1544-1564.

Keyword	Reference
Hogan (2008)	Hogan, R. J., (2008): Fast lidar and radar multiple-scattering models – 1. Small-angle scattering using the photon variance-covariance method. *J. Atmos. Sci.,* in press.
Hogan and Illingworth (1999)	Hogan, R. J., and A. J. Illingworth (1999), The potential of spaceborne dual-wavelength radar to make global measurements of cirrus clouds, *J. Atmos Oceanic. Technol.*, *16*, 518--531.
Hogan and Kew (2005)	Hogan, R. J., and S. F. Kew (2005), A 3D stochastic cloud model for investigating the radiative properties of inhomogeneous cirrus clouds. *Q. J. R. Meteorol. Soc., 131,* 2585-2608.
Hogan et al. (2003)	Hogan, R. J., P. N. Francis, H. Flentje, A. J. Illingworth, M. Quante and J. Pelon (2003), Characteristics of mixed-phase clouds – 1. Lidar, radar and aircraft observations from CLARE'98. *Quart. J. Roy. Meteorol. Soc., 129,* 2089-2116.
Hogan et al. (2006a)	Hogan, R. J., M. P. Mittermaier, and A. J. Illingworth (2006a), The retrieval of ice water content from radar reflectivity factor and temperature and its use in the evaluation of a mesoscale model, *J. Appl. Meteorol. Climatology*, *45*, 301-317.
Hogan et al. (2006b)	Hogan, R. J., D. P. Donovan, C. Tinel, M. A. Brooks, A. J. Illingworth, and J. P. V. Poiares Baptista (2006b), Independent evaluation of the ability of spaceborne radar and lidar to retrieve the microphysical and radiative properties of ice clouds, *J. Atmos Oceanic. Technol.*, *23*, 211-227.
Hogan and Battaglia (2008)	Hogan, R. J., and A. Battaglia (2008), Fast lidar and radar multiple-scattering models - 2. Wide-angle scattering using the time-dependent two-stream approximation, *J. Atmos. Sci.,* in press.
Hollingsworth and Lönnberg (1986)	Hollingsworth, A., and P. Lönnberg (1986), The statistical structure of short-range forecast errors as determined from radiosonde data. Part I: The wind field, *Tellus*, *38A*, 111--136.
Illingworth et al. (2000)	Illingworth, A. J., R. J. Hogan, A. C. A. P. van Lammeren, D. P. Donovan, F. H. Berger, T. Halecker, C.-L. Liu, A. Feijt, and H. I. Bloemink (2000), Quantification of the synergy aspects of the Earth Radiation Mission, final report, ESTEC Contract 13167/98/NL/GD. http://www.met.rdg.ac.uk/clouds/publications/synergy.pdf.
Kato et al. (1999)	Kato, S., T. P. Ackerman, J. H. Mather, and E. E. Clothiaux (1999), The k-distribution method and correlated-k approximation for a shortwave radiative transfer model, *J. Quant. Spectrosc. Radiat. Transfer, 62,* 109– 121.
Liebe (1985)	Liebe, H. J. (1985), An updated model for millimeter-wave propagation in moist air, *Radio Science*, *20*, 1069--1089.

Keyword	Reference
Liu and Illingworth (2000)	Liu, C. L., and A. J. Illingworth (2000), Towards more accurate retrievals of ice water content from radar measurement of clouds, *J. Appl. Meteorol.*, *39*, 1130--1146.
Mitchell (2006)	Mitchell, D. (2006), Use of mass- and area-dimensional power laws for determining precipitation particle terminal velocity, J. Atmos. Sci., 53, 1710–1723.
Morcrette (2001)	Morcrette, J.-J. (2001), Accessment of the ECMWF model cloudiness and surface radiation fields at the ARM-SGP site. ECMWF technical memorandum.
Platt et al. (1987)	Platt, C. M. R., S. C. Scott, and A. C. Dilley (1987), Remote sounding of high clouds - 4. Optical properties of midlatitude and tropical cirrus, *J. Atmos. Sci.*, *44*, 729--747.
Platt et al. (2002)	Platt, C. M. R., S. A. Young, R. T. Austin, G. R. Patterson, D. L. Mitchell, and S. D. Miller (2002), LIRAD Observations of Tropical Cirrus Clouds in MCTEX. Part I: Optical Properties and Detection of Small Particles in Cold Cirrus, J. Atmos.Sci., 59, 3145–3162.
Protat et al. (2007)	Protat, A., J. Delanoë, D. Bouniol, A. J. Heymsfield, A. Bansemer, and P. R. A. Brown (2007), Evaluation of ice water content retrievals from cloud radar reflectivity and temperature using a large airborne in-situ microphysical database, *J. Appl. Meteorol.*, *46*, 5, 557--572.
Rodgers (2000)	Rodgers, C. D. (2000), *Inverse methods for atmospheric sounding: Theory and practice*, 238 pp., World Scientific.
Saunders et al. (1999)	Saunders, R., M. Matricardi, and P. Brunel, 1999: An improved fast radiative transfer model for assimilation of satellite radiance observations. *Quart. J. Roy. Meteorol. So., 125,* 1407-1425.
Tinel et al. (2005)	Tinel, C., J. Testud, R. J. Hogan, A. Protat, J. Delanoë, and D. Bouniol (2005), The retrieval of ice cloud properties from cloud radar and lidar synergy, *J. App. Meteorol.*, *44*, 860--875.
Toon et al. (1989)	Toon, O. B., C. P. McKay, T. P. Ackerman, and K. Santhanam (1989), Rapid calculation of radiative heating rates and photodissociation rates in inhomogeneous multiple scattering atmospheres, *J. Geophys. Res., 94,* 16,287– 16,301.